RSC Applied Interfaces

ROYAL SOCIETY OF CHEMISTRY

PAPER

View Article Online
View Journal | View Issue

Cite this: *RSC Appl. Interfaces*, 2025, **2**, 1850

Synergistic effect of a one-pot synthesised kaolinite–cerium melamine cyanurate hybrid for an improved metal protective coating

Nithyaa Jayakumar [ab] and Nishanth Karimbintherikkal Gopalan *[ab]

Received 1st July 2025,
Accepted 25th September 2025

DOI: 10.1039/d5lf00189g

rsc.li/RSCApplInter

This paper presents the cerium–melamine cyanurate (CeMC) complex as an anticorrosive pigment prepared by one-pot synthesis. Further, kaolinite is integrated to prepare KCeMC to improve the barrier performance of the anticorrosive coating. The effectiveness of the synthesised pigment-loaded epoxy coatings was assessed using electrochemical impedance spectroscopy in a 3.5 wt% NaCl solution. X-ray photoelectron spectroscopy (XPS) and scanning electron microscopy with energy-dispersive X-ray spectroscopy (SEM-EDX) confirmed the release of the cathodic inhibitor Ce^{3+}, which forms a protective layer over defective areas of the coating. A five-fold increase in the initial coat resistance was observed compared to the pristine epoxy, as measured by electrochemical impedance spectroscopy (EIS). A 1 wt% KCeMC loaded epoxy coating reveals better durability among all the synthesised pigment loaded coatings. The impedance results exhibited remarkable long-term durability, maintaining a high coating resistance of 7.70×10^9 Ω cm^2 after 2 months of immersion in a saline medium. The improved protective properties of the epoxy coating containing KCeMC are attributed to the synergistic effects of cerium inhibition along with the barrier performance provided by kaolinite and melamine cyanurate.

Introduction

Effective corrosion inhibition of cerium salts has been studied across various metal surfaces, including aluminium alloys, steel, and magnesium alloys.[1] Hybrid systems are developed by combining cerium-based inhibitors with complementary barrier components, resulting in a synergistic protective effect and enhanced corrosion resistance. Owing to their superior protective performance and environmental compatibility, hybrids of cerium compounds are widely employed in metal protective coatings.[2,3] Cerium-based compounds create a protective barrier by precipitating as insoluble cerium oxide or hydroxide at cathodic sites, thereby blocking oxygen reduction and suppressing the corrosion process.[4] In recent decades, research in surface engineering and protective coatings has increasingly focused on cerium-based corrosion inhibition.

Cerium-based hybrids with organic compounds have demonstrated synergistic protective performance, as reported in various studies. Dong *et al.* developed an epoxy coating incorporating cerium oxide modified with fumaric acid as an effective corrosion inhibitor.[5] Chen *et al.* investigated cerium tartrate within an epoxy matrix, analysing its inhibition mechanism through X-ray photoelectron spectroscopy (XPS) and inductively coupled plasma mass spectrometry (ICP-MS).[6] Seyyed Arash Haddadi *et al.* explored a cerium-doped, tannic acid-reduced graphene oxide nanocomposite, which induced a cross-linked, dense epoxy formulation offering dual mechanical reinforcement and corrosion protection.[7] Shi *et al.* evaluated the deposition of cerium cinnamate on AA 2024-T3, followed by hydrolysis of cerium ions to form protective cerium oxide/hydroxide layers.[8] Mardel *et al.* examined the use of cerium dibutyl phosphate to mitigate filiform corrosion, while Soestbergen *et al.* analysed the sustained release behaviour of Ce^{3+} ions from cerium dibutyl phosphate coatings.[9,10] The research outcomes underscore the promising potential of combining cerium with organic compounds to enhance the protective performance of organic coatings.

Melamine with different organic acids resulted in self-assembly *via* non-covalent interactions, leading to 3D architectures.[11,12] Melamine cyanurate is one of the most studied compounds in molecular engineering due to its wide application.[13–15] Melamine cyanurate supramolecular co-crystals/complexes resulted from the complementary hydrogen bonding between melamine (organic base) and cyanuric acid (organic acid).[16] Coordination sites of nitrogen

[a] *Centre for Sustainable Energy Technologies, CSIR-National Institute for Interdisciplinary Science and Technology (NIIST), Thiruvananthapuram 695019, India. E-mail: nishanthkg.niist@csir.res.in; Fax: +91471 2491712; Tel: +91471 2515508*
[b] *Academy of Scientific and Innovative Research (AcSIR), Ghaziabad-201002, India*

and oxygen in melamine cyanurate prefer to form coordination complexes with cerium ions in the current work.

The point of focus of the current work is to reveal the protective performance of epoxy coatings with the kaolinite integrated cerium–melamine cyanurate complex. Kaolinite addition is projected to strengthen the barrier function of the coating. The corrosion resistance of the developed coatings was examined in 3.5 wt% NaCl solution using electrochemical impedance spectroscopy (EIS). Active corrosion inhibition was showcased with the assistance of XPS and SEM-EDX analysis. In summarising the current study, the kaolinite integrated cerium–melamine cyanurate coordination complex can considerably improve the durability of coatings in saline media.

Experimental section

Materials

Cerium nitrate, melamine, cyanuric acid and kaolinite were purchased from Sigma-Aldrich Chemical Company with 99.999% purity. Epoxy and its respective polyamide hardener were purchased from Aditya. Sodium chloride and *n*-butyl alcohol were purchased from Merck. Experiments were carried out using locally procured steel specimens with the following chemical composition (wt%): C = 0.24, Mn = 0.92, Al = 0.03, Si = 0.14, Cr = 0.04, V = 0.10, P = 0.08, Cu = 0.06, and balance Fe.

Pigment synthesis

The melamine cyanurate (MC) supramolecular complex was synthesised *via* a conventional precipitation route using a 1:1 molar ratio of melamine to cyanuric acid.[17,18] Cynurate solution was slowly added dropwise into the melamine solution for the gradual nucleation of MC under ambient conditions.

A similar precipitation procedure was adopted in the presence of cerium nitrate (5 wt%) to form a cerium–melamine cyanurate coordination complex (CeMC). First, cerium nitrate solution was added to the melamine solution, and then cyanuric acid was added to the mixture, resulting in the precipitation of CeMC.

To enhance the barrier property of the synthesised pigment, kaolinite was incorporated during the precipitation process of CeMC, resulting in the formation of a kaolinite-integrated CeMC (KCeMC). Kaolinite (1 wt%) was dispersed in the cerium nitrate and melamine mixture solution using probe sonication, followed by precipitation with cyanuric acid under ambient conditions. Finally, the precipitate was stirred for 3 h, thoroughly washed, collected by centrifugation, and

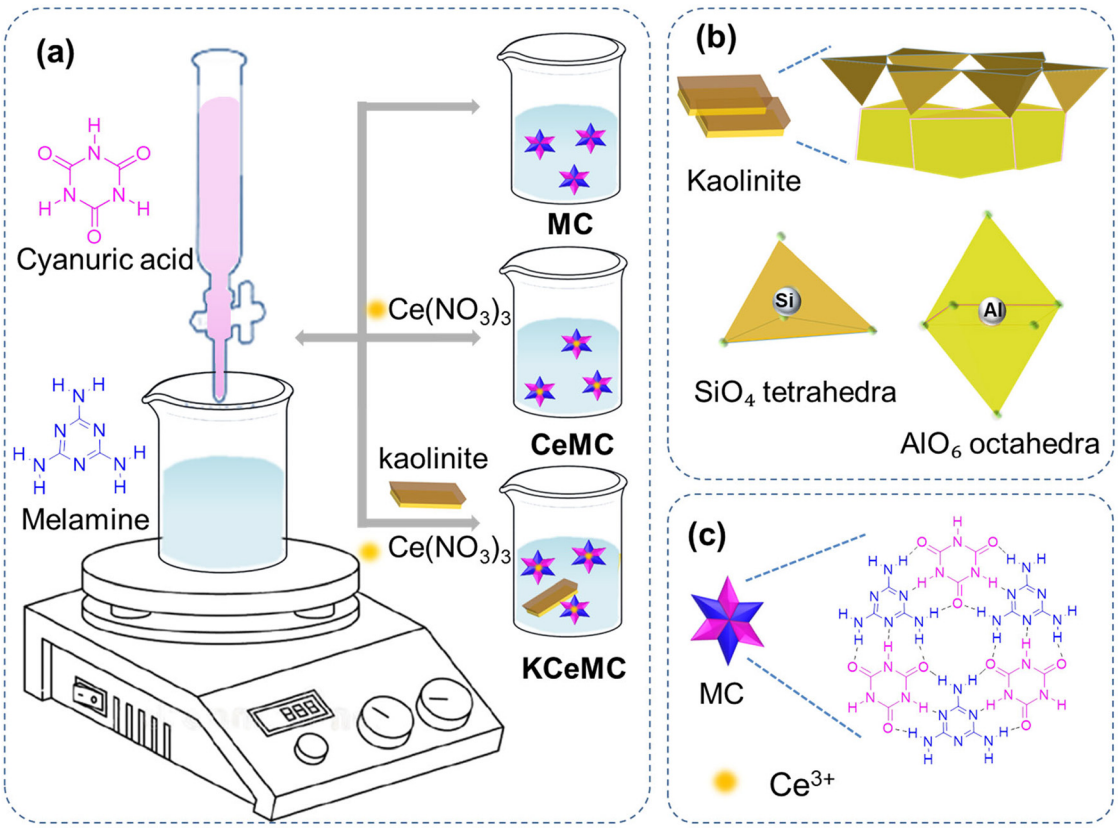

Fig. 1 (a) Schematic representation of the synthesis process of MC, CeMC and KCeMC, (b) 1:1 layered kaolinite structure formed by silica tetrahedral and alumina octahedral sheets and (c) schematic illustrating MC with alternating complementary H-bonds between melamine and cyanuric acid.

dried overnight at 60 °C. The schematic illustration of all the synthesised pigments is shown in Fig. 1.

Coating preparation

The steel coupon with 40 × 30 mm dimensions was polished with different grades of emery paper in ascending order of grit up to 1500, followed by degreasing with acetone. Subsequently, coupons were coated using the dip coating method.

Pristine coating solution was composed of an epoxy binder, polyamide hardener and tertiary butanol solvent in a weight ratio of 2 : 1 : 2. The final coating formulation contained 1 wt% of synthesised pigments incorporated in the epoxy matrix to prepare MC/epoxy, CeMC/epoxy and KCeMC/epoxy coatings.

Dipcoating with a rate of 10 mm min^{-1} with an immersion time of one minute was adapted to achieve a coating thickness of approximately 15 μm. Coated coupons are allowed to cure for 48 hours under ambient conditions. The coating thickness was confirmed using a profilometer. Three coupons were prepared using the same coating formulation to ensure the concurrent resistance of the coating.

Characterisation

A Bruker Alpha-T Fourier transform infrared spectrometer (FT-IR), with a spectral resolution of 4 cm^{-1} across a wavelength range of 400–4000 cm^{-1}, was used to study the molecular structure of the synthesised pigment. For the analysis, the dried pigment powder was finely ground, mixed with spectroscopic grade KBr, and pressed into pellets prior to measurement. The phase composition of the synthesised pigment was analysed using powder X-ray diffraction (PXRD) patterns obtained with a Philips X'pert Pro diffractometer, employing Ni-filtered Cu-Kα radiation (λ = 1.541 Å). The pigments were finely ground and then evenly spread on a zero-background holder (silicon) to ensure a flat surface for accurate diffraction measurements. The electronic configuration and surface composition of the synthesised hybrid anticorrosive pigments and microanodic region were examined using X-ray photoelectron spectroscopy (XPS) performed on a PHI 5000 Versa Probe II system (ULVAC-PHI Inc., USA), equipped with a micro-focused (100 μm, 15 kV) monochromatic Al-Kα X-ray source ($h\nu$ = 1486.6 eV). For XPS analysis, the dried pigment powders were pressed onto double-sided conductive carbon tape mounted on the sample stub, and the surfaces were gently blown with nitrogen gas to remove any loosely attached particles. The analysis spot was selected on a smooth, uniform region of the sample to avoid surface irregularities and ensure representative spectra. An ULVAC-PHI Versaprobe II instrument was equipped with a patented dual-beam charge neutralisation system. This system employs a combination of low-energy electrons and ions to compensate for positive charge buildup during analysis of insulating samples, thereby improving spectral accuracy. The raw spectra were background-corrected using a Shirley background, and all curve fitting was carried out in CasaXPS software with appropriate constraints. Binding energies were calibrated with respect to the C 1s carbon peak at 284.6 eV. The quality of the fits was evaluated using residual standard deviations (STDs), which were consistently less than 0.05, confirming the robustness of the fitting procedure. The microscopy investigation was conducted using a field emission scanning electron microscope (FESEM), model JEOL JSM5600. For FESEM analysis, the dried hybrid pigment powder was evenly spread on conductive carbon tape mounted on an aluminum stub and sputter-coated with a thin layer of gold to avoid charging effects during imaging. Further, detailed micrographical investigation of synthesised hybrid materials was investigated using a transmission electron microscope (TEM) coupled with an energy-dispersive X-ray spectroscopy (EDX) system, employing a JEOL JEM F-200 microscope operating at 200 kV. For TEM analysis, a small amount of the dried hybrid pigment powder was ultrasonically dispersed in ethanol, and a drop of the suspension was deposited onto a carbon-coated copper grid. The solvent was allowed to evaporate under ambient conditions before imaging. The thickness was determined using a surface profilometer by creating a scratch through the coating to the substrate and recording the step height across the scratch. Multiple measurements were taken at different locations to ensure reproducibility, and the average coating thickness is approximately 15 μm.

The corrosion resistance and inhibition performance of the synthesised pigment-loaded epoxy coating on steel coupons were analysed in 3.5 wt% NaCl solution using Electrochemical Impedance Spectroscopy (EIS). The results were compared with those of the individual components in the hybrid system and pristine epoxy coating. The analysis was conducted using a Metrohm Autolab M204 electrochemical potentiostat workstation (The Netherlands). The electrochemical corrosion cell consists of a coated steel coupon with a 1 cm^2 exposed area as the working electrode, a saturated calomel electrode (SCE) as the reference electrode, and graphite as the counter electrode. Impedance measurements were performed at the steady-state open circuit potential (OCP), with a 0.005 V AC signal applied over a frequency range of 10^5 to 10^{-2} Hz. To ensure reliable results, the procedure was repeated three times with different coated coupons. The raw EIS data were analysed using ZSimpWin software, which applied an electrochemical equivalent circuit to extract and interpret the electrochemical parameters.

Results and discussion

Phase identification and functional group analysis

The X-ray diffraction pattern of pristine kaolinite, along with the synthesised pigments, is illustrated in Fig. 2a. In order to clearly illustrate the peak shift, the magnified diffraction patterns are presented in Fig. 2b–e. The synthesised MC aligns with the reference code JCPDS No: 00-005-0127.[19–22] In

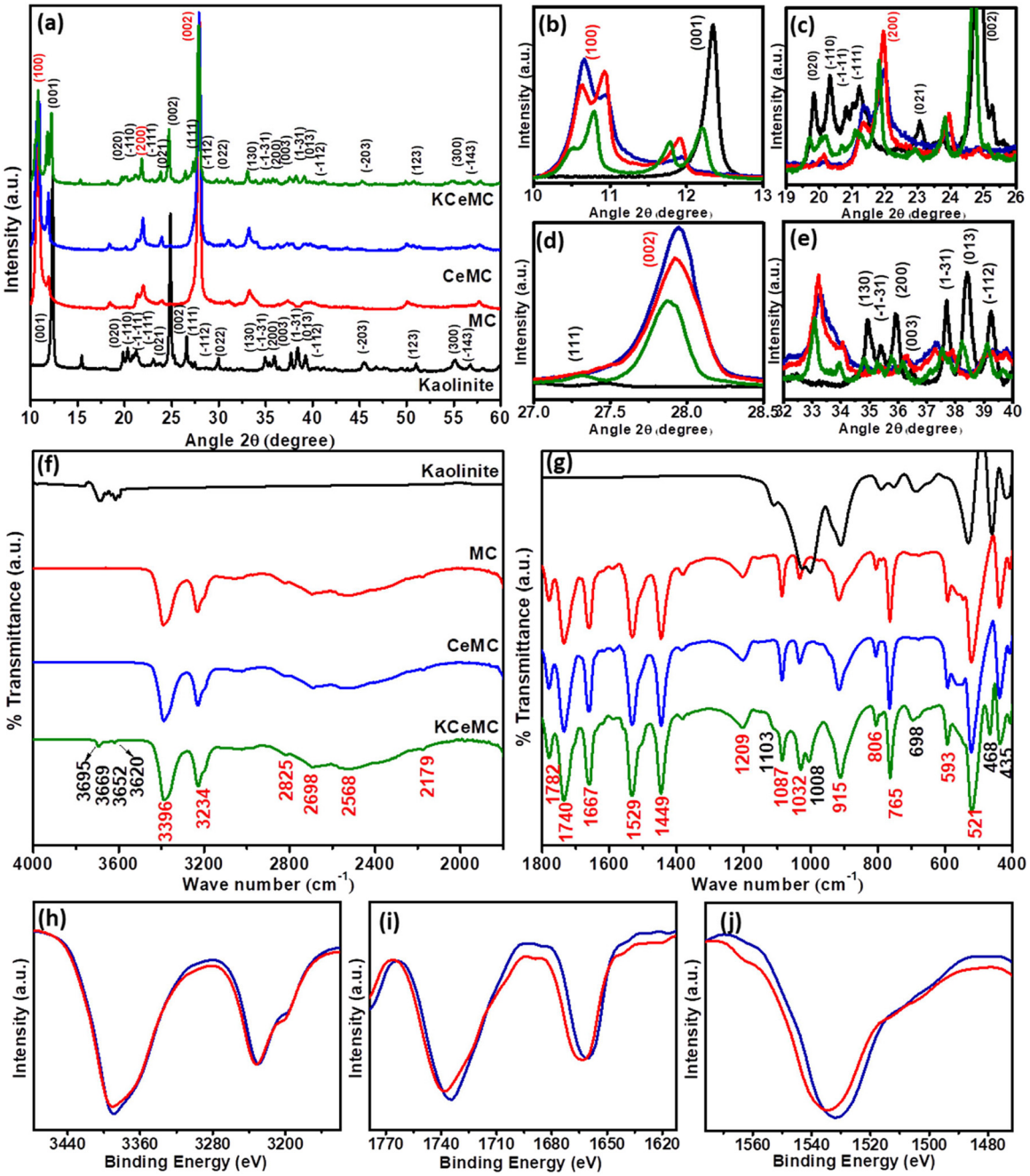

Fig. 2 (a–e) XRD patterns and (f–j) IR bands of kaolinite, MC, CeMC and KCeMC.

the case of CeMC, there is a noticeable slight peak shift towards the lower two theta values, which can be attributed to the interaction between cerium and the MC molecular complex. When kaolinite is introduced into KCeMC, the diffraction pattern displays contributions from both kaolinite, referenced by JCPDS code 00-005-0143, and MC, also exhibiting a lower two-theta shift. This peak shift may indicate variations in the interlayer structure, an increase in intercalation, or changes in the stacking of CeMC on the kaolinite surface.[23]

The IR analysis revealed several significant vibrational modes related to the functional groups present in the synthesised hybrid pigment (Fig. 2f and g). Fig. 2h–j clearly demonstrates a shift in the vibrational bands of melamine cyanurate upon coordination with Ce^{3+} ions. In pristine melamine cyanurate, vibrational band corresponding to hydrogen-bonded amino and imino groups within the triazine–cyanurate network. However, upon the coordination of Ce^{3+}, the bands displaced to lower wavenumbers, indicative of red shift, is typically attributed to metal–ligand interactions, wherein Ce^{3+} coordinates with electronegative heteroatoms (–NH_2 and –C═O groups) of the melamine cyanurate framework. This coordination weakens bond strength by delocalising the electron density

toward the metal centre, lowering the vibrational frequency. The observed spectral changes thus provide strong evidence for the involvement of the amino and carbonyl functionalities of melamine cyanurate in Ce^{3+} coordination. The vibration band at 3396 cm^{-1} is attributed to the symmetric stretching vibration of $-NH_2$ groups in the triazine ring, and the band at 3234 cm^{-1} with low frequency shoulder corresponds to N–H stretching modes that are more strongly hydrogen bonded between amino and imino groups.[24,25] The N–H stretching and asymmetric stretching features are observed at 2825 cm^{-1} and at 2698 cm^{-1}.[24] A strong absorption at 1782 cm^{-1} is characteristic of the C═O stretching vibration of cyanuric acid carbonyl groups, whereas the band at 1667 cm^{-1} arises from $-NH_2$ bending vibrations.[26] The peak at 1529 cm^{-1} corresponds to the C═N stretching of the triazine ring, with further C–N symmetric stretching contributions observed at 1449 and 1209 cm^{-1}.[24] Characteristic triazine skeletal vibrations are evident at 1032 and 915 cm^{-1}, while the bands at 806 and 765 cm^{-1} are attributed to the out-of-plane bending of the triazine ring.[24] At lower frequencies, the band near 593 cm^{-1} is assigned to ring bending, and the absorption at 521 cm^{-1} corresponds to the in-plane C–N bending vibration of the side chain. These vibration modes confirm the typical melamine cyanurate formation in KCeMC.

The presence of kaolinite is confirmed by the vibrational bands observed in KCeMC. Specifically, the stretching frequency of the hydroxyl (OH) bands reveals four distinct stretching bands at 3620, 3653, 3670, and 3695 cm^{-1}.[27,28] Additionally, the band at 1130 cm^{-1} is attributed to Si–O stretching vibrations, while the absorptions at 1032 and 1008 cm^{-1} correspond to the anti-symmetric stretching of equatorial Si–O bonds.[29] The feature observed at 698 cm^{-1} can be assigned either to Si–O stretching or to Al–OH deformation modes. At lower frequencies, the bands at 468 and 435 cm^{-1} are characteristic of O–Si–O and O–Al–O bending vibrations.[27,30]

Investigation of surface composition and oxidation states

Furthermore, XPS analysis of the binding energies of valence electrons was employed to establish the surface chemical composition of the synthesised pigments. The elemental presence in KCeMC (C, N, O, Ce, Al and Si) was confirmed from the full scan (survey spectra) as shown in Fig. 3a. Fig. 3b–g show the deconvoluted high-resolution XPS spectra of C 1s, N 1s, O 1s, Ce 3d, Al 2p and Si 2p. KCeMC has significant peaks that confirm the typical pattern of melamine cyanurate reported in the literature.[31–33]

The C 1s core spectra are deconvoluted into three distinct peaks that relate to different types of bonding. The peaks are observed at 284.3 eV for C–C/C–H bonds, 286.3 eV for C–N═C bonding in the triazine ring, and 288.2 eV for the carbonyl group found in cyanuric acid[31] (Fig. 3b).

Similarly, the high-resolution nitrogen 1s spectrum reveals three significant peaks upon deconvolution. The first peak, observed at 398.7 eV, corresponds to sp^2 nitrogen from C–N═C bonds within the triazine rings of both melamine and cyanuric acid. 398.8 eV is the peak attributed to the amino groups present in melamine. Lastly, a peak at 401.1 eV is generated due to hydrogen bonding interactions[31–33] (Fig. 3c).

In the O 1s spectrum, a deconvoluted peak appears at 530.2 eV, attributed to the aluminium silicate framework. This is followed by a peak at 531.3 eV for the carbonyl group in melamine cyanurate, a peak at 532.2 eV related to the –OH group attached to kaolinite, and another peak at 533.5 eV, corresponding to adsorbed water molecules on KCeMC[33,34] (Fig. 3d).

The 3d spectrum reveals ten characteristic peaks resulting from the spin–orbit splitting of Ce $3d_{5/2}$ and Ce $3d_{3/2}$. These peaks, labelled from V^0 to U^{III}, include distinct peaks for V^0, V^I, U^0, and U^I, which indicate the presence of the Ce^{3+} oxidation state. The remaining six peaks are associated with the Ce^{4+} oxidation state, with the intense Ce^{3+} peaks highlighting a rich abundance of the 3+ oxidation state[4,27] (Fig. 3e).

Finally, the Al 2p and Si 2p peaks emerge around 74.3 eV and 102.4 eV, respectively, corresponding to Al–O bonds in AlO_6 octahedra and Si–O bonds in SiO_4 tetrahedra of kaolinite[35] (Fig. 3f and g).

Microstructural analysis

SEM analysis confirmed the characteristic flake-like morphology of CeMC (Fig. 4a). High-resolution TEM analysis was performed further to examine the internal structure and fine morphological details. The TEM image of CeMC in Fig. 4b revealed well-defined nanoflakes in CeMC. Selected area electron diffraction of CeMC provides concentric ring patterns that confirm the polycrystalline nature of the material[36] (Fig. 4c).

In the KCeMC hybrid pigment, CeMC nanoflakes were uniformly distributed on kaolinite microsheets, as shown in Fig. 4d. The TEM image of KCeMC in Fig. 4e shows defined nanoflakes in CeMC and their homogeneous dispersion across kaolinite surfaces in KCeMC.

KCeMC exhibits the concentric ring patterns of CeMC as well as diffraction spots of kaolinite, confirming the hybrid nature of the compound[27] (Fig. 4f). Complementary Electron Energy Loss Spectroscopy (EELS) analysis confirmed the spatial distribution of C, N, O, Ce, Al, and Si elements within the KCeMC structure.

The suggested mechanism of the synthesised KCeMC pigment is shown in Fig. 5. The complementary hydrogen bonding between the keto group and triazine ring drives the supramolecular network MC formation. The addition of a cerium precursor during the MC precipitation leads to the coordination of cerium with MC. The formation of KCeMC, resulting from the precipitation of CeMC onto kaolinite, was

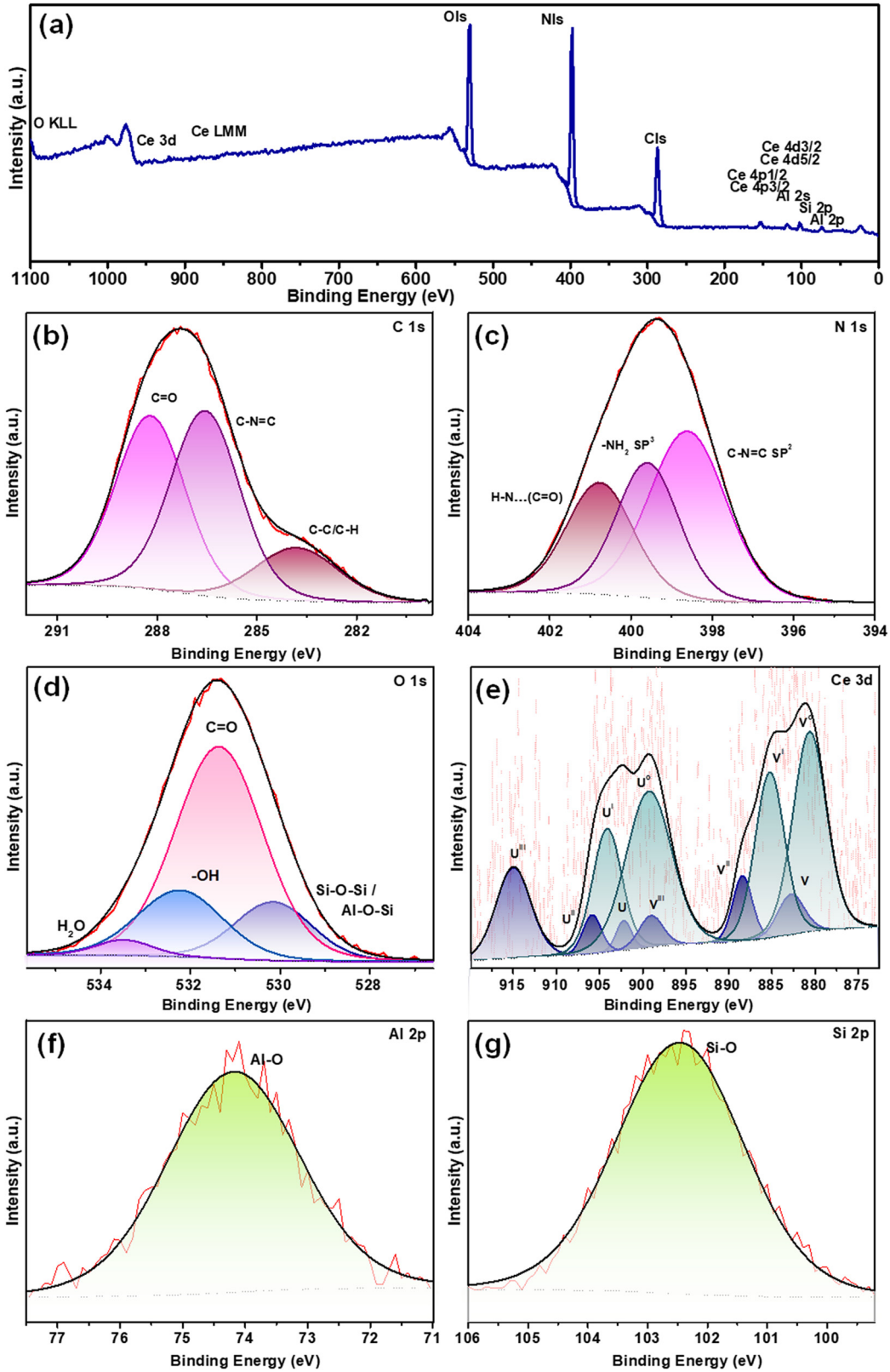

Fig. 3 Surface chemistry of the synthesised KCeMC pigment analysed by XPS: (a) survey spectra and high-resolution spectra of (b) C 1s, (c) N 1s, (d) O 1s, (e) Ce 3d, (f) Al 2p and (g) Si 2p.

substantiated by characteristic shifts in diffraction patterns and IR absorption bands, complemented by surface compositional analysis using XPS and morphological characterisation through microstructural imaging.

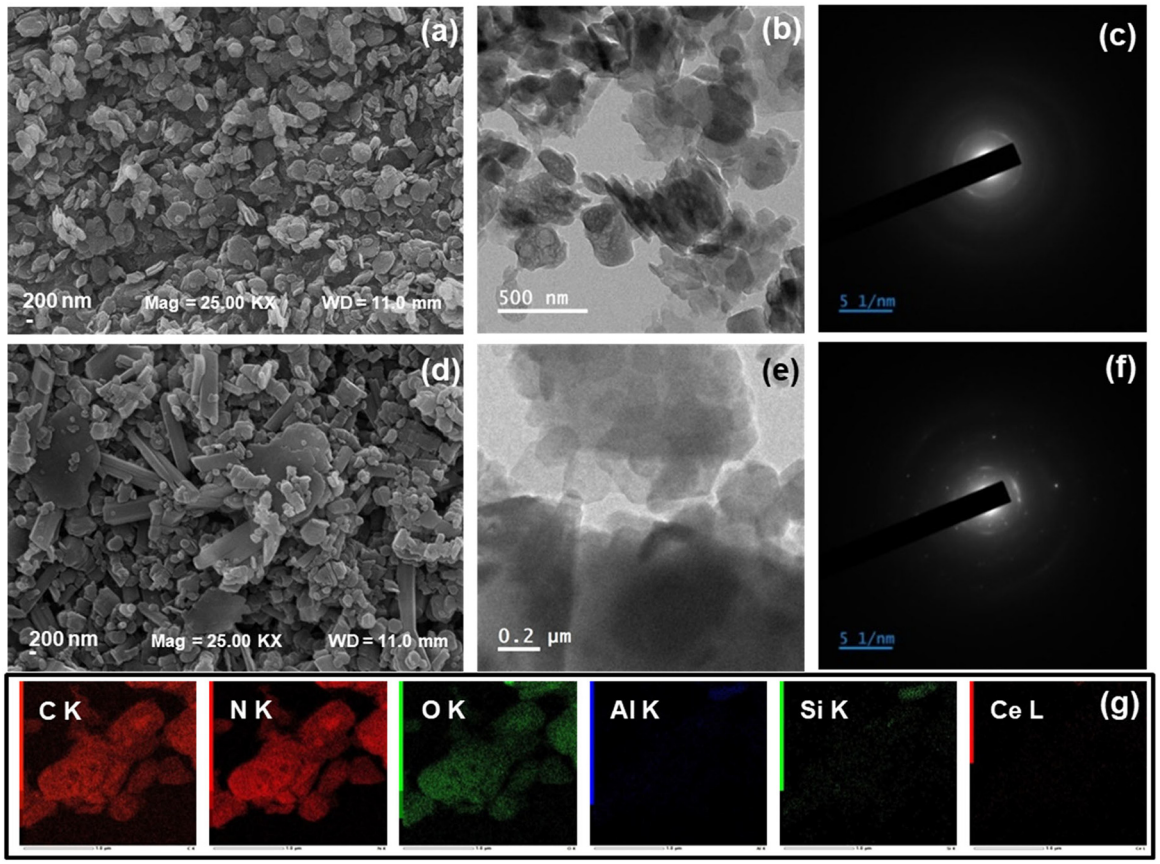

Fig. 4 (a) SEM image, (b) TEM image and (c) SAED pattern of CeMC. (d) SEM image, (e) TEM image and (f) SAED pattern of KCeMC and (g) EELS elemental distribution maps of C, N, O, Ce, Al and Si of KCeMC.

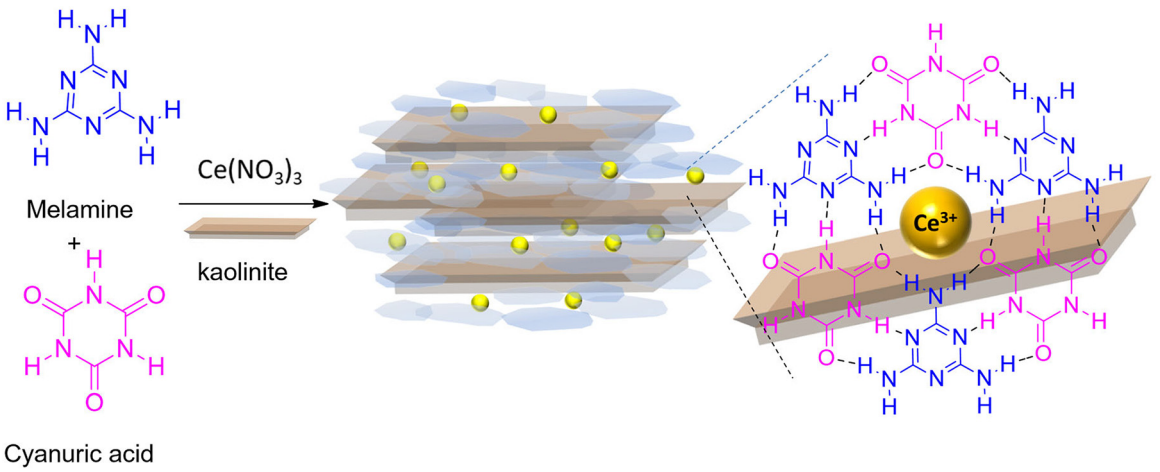

Fig. 5 Proposed schematic representation of the formation mechanism of KCeMC.

Electrochemical assessment of protective performance

The protective nature of the synthesised anticorrosive pigment-loaded anticorrosive coating formulations was evaluated using EIS analysis, and the results are summarised in Table 1. The passive elements deconvoluted from the raw EIS data, such as coat resistance (R_c), charge transfer resistance (R_{ct}), coat capacitance (Q_c) and double layer capacitance (Q_{dl}), provide insight into the protective performance of the coating in a saline environment.[37] A low charge transfer resistance of 1200 Ω cm^2 of the bare steel specimen indicates the aggressive corrosion of the steel in 3.5 wt% NaCl solution (Fig. 6a). The OCP values for the KCeMC coated specimens were significantly more positive than that of the bare steel (−0.67 V *vs.* SCE), which confirms

Table 1 Summary of passive elements deconvoluted from EIS measurements

Sample	Duration	R_c (Ω cm^2)	Q_c		R_{ct} (Ω cm^2)	Q_{dl}	
			Y_o (Ω^{-1} cm^{-2} S^n)	n_1		Y_o (Ω^{-1} cm^{-2} S^n)	n_2
Bare metal	—	—	—	—	1.20×10^3	—	—
Bare epoxy	1 day R(Q(R(QR)))	1.63×10^5	2.72×10^{-7}	0.7	2.05×10^6	1.13×10^{-6}	0.6
Epoxy–kaolinite	1 day R(QR)	1.37×10^9	2.18×10^{-8}	0.8	—	—	—
Epoxy–MC	1 day R(Q(R(QR)))	1.36×10^7	2.36×10^{-8}	0.9	7.27×10^9	8.05×10^{-9}	0.8
Epoxy–CeMC	1 day R(QR)	1.14×10^{10}	2.49×10^{-10}	0.8	—	—	—
	1 week R(Q(R(QR)))	3.83×10^8	2.40×10^{-10}	0.9	7.41×10^9	3.09×10^{-9}	0.8
	1 month R(Q(R(QR)))	3.12×10^8	2.89×10^{-10}	0.9	4.27×10^9	4.55×10^{-9}	0.6
Epoxy–KCeMC	1 day R(QR)	1.10×10^{11}	1.84×10^{-10}	0.9	—	—	—
	1 week R(QR)	5.67×10^{10}	2.68×10^{-10}	0.9	—	—	—
	1 month R(QR)	3.05×10^{10}	4.25×10^{-10}	0.9	—	—	—
	2 months R(QR)	7.70×10^9	3.05×10^{-10}	0.9	—	—	—

the passive nature of the coatings. Throughout the exposure period, the OCP values remained consistently positive with minimal variation. Initially, the OCP ranged from 0.5 V to 0.2 V, and after two months, it ranged from 0.05 V to 0.01 V for all the prepared KCeMC–epoxy coated coupons.

Variations in the formulation of the epoxy matrix can significantly influence the Nyquist response. Changes in composition alter the barrier characteristics, electrochemical behaviour, and corrosion resistance of the coating, as well as its interaction with the electrolyte. These factors govern the ability of the coating to impede the ingress of corrosive ions and determine its interfacial electrochemical behaviour upon contact with the steel substrate. Consequently, such modifications directly affect the overall impedance magnitude and the characteristic shape of the Nyquist plots. Fig. 6 presents the Nyquist plots of bare epoxy, kaolinite and synthesised pigments.

To demonstrate the enhanced coating performance in terms of higher impedance values and reduced water uptake, the formulated epoxy coatings were systematically compared against pristine epoxy coatings. This comparative analysis highlights the effectiveness of the pigments in improving the barrier properties and corrosion resistance of the coating system. The pristine epoxy exhibits an R_c of 1.63×10^5 Ω cm^2 and an R_{ct} of 2.05×10^6 Ω cm^2 due to the inherent defects in the coating (Fig. 6b). The individual components, kaolinite and MC incorporated epoxy coating formulation, were evaluated to justify the quantitative importance of the requirement for hybrid pigments (Fig. 6c and d).

Among the synthesised pigment-reinforced formulated coatings, epoxy–KCeMC demonstrated the most remarkable performance. After 1 day of exposure in 3.5 wt% NaCl solution, epoxy–KCeMC exhibits a coat resistance of 1.10×10^{11} Ω cm^2, superior to epoxy–CeMC and epoxy–MC (1.14×10^{10} and 1.36×10^7 Ω cm^2). Meanwhile, there is a gradual decline in R_c of epoxy–KCeMC to 5.67×10^{10} Ω cm^2 after 1 week, 3.05×10^{10} Ω cm^2 after one month and 4.26×10^9 Ω cm^2 even after two months of continuous exposure (Fig. 6e and f). Upon continuous exposure of epoxy–CeMC for 1 week, R_c declined to 3.83×10^8 Ω cm^2 and after 1 month of exposure, it resulted in 3.12×10^8 Ω cm^2. The high R_{ct} value after one week (7.41×10^9 Ω cm^2) and not much decline after one month of exposure (4.27×10^9 Ω cm^2) suggest that the electrochemical reaction at the metal coat interface was strongly impeded (Fig. 6g and h). In comparison, the poor initial performance of epoxy–MC shows the role of cerium incorporation.

Overall, the kaolinite and cerium incorporation resulted in the enhanced performance, which was revealed from the absence of R_{ct} even after two months of saline exposure in the epoxy–KCeMC coating. Fig. 6i and j present the schematic illustrations of an equivalent electrochemical circuit model applied to interpret the experimental impedance data. The epoxy–MC and epoxy–kaolinite coatings showed Q_c values of 2.36×10^{-8} Ω^{-1} cm^{-2} s^n and 2.18×10^{-8} Ω^{-1} cm^{-2} s^n respectively, better than that of bare epoxy (2.72×10^{-7} Ω^{-1} cm^{-2} s^n), indicating the increased diffusion pathway of the coating. In comparison, epoxy–CeMC and epoxy–KCeMC with a stable Q_c of 10^{-10} Ω^{-1} cm^{-2} s^n indicate enhanced barrier performance against the electrolyte penetration to reach the metal/coat interface. The Q_c is aligned with the R_c and R_{ct} results of the coating. This outstanding performance is attributed to the synergistic barrier effect of kaolinite microsheets, melamine cyanurate nanoflakes and the corrosion-inhibitive action of cerium, effectively enhancing the corrosion resistance of the epoxy/KCeMC coating system.

Evaluation of corrosion protection behaviour at induced defects in the coating

Definitive evidence for the active performance of KCeMC, a defect of 10 mm long and 15 μm deep (matching the coating thickness), was obtained using a surgical knife. The detailed chemical state of the protective layer was evaluated using XPS analysis after 48 h exposure to a saline environment. Fig. 7a displays the photoemission broad spectra of the inhibitive layer in the defective region. The existing elements were detected from the survey spectrum. The binding energy of the photoelectrons emitted from the inhibitive film ensures the presence of Fe, O and P, which matches the XRD results. The core spectra of the elements were deconvoluted with the assistance of CasaXPS software. The XPS results reveal the

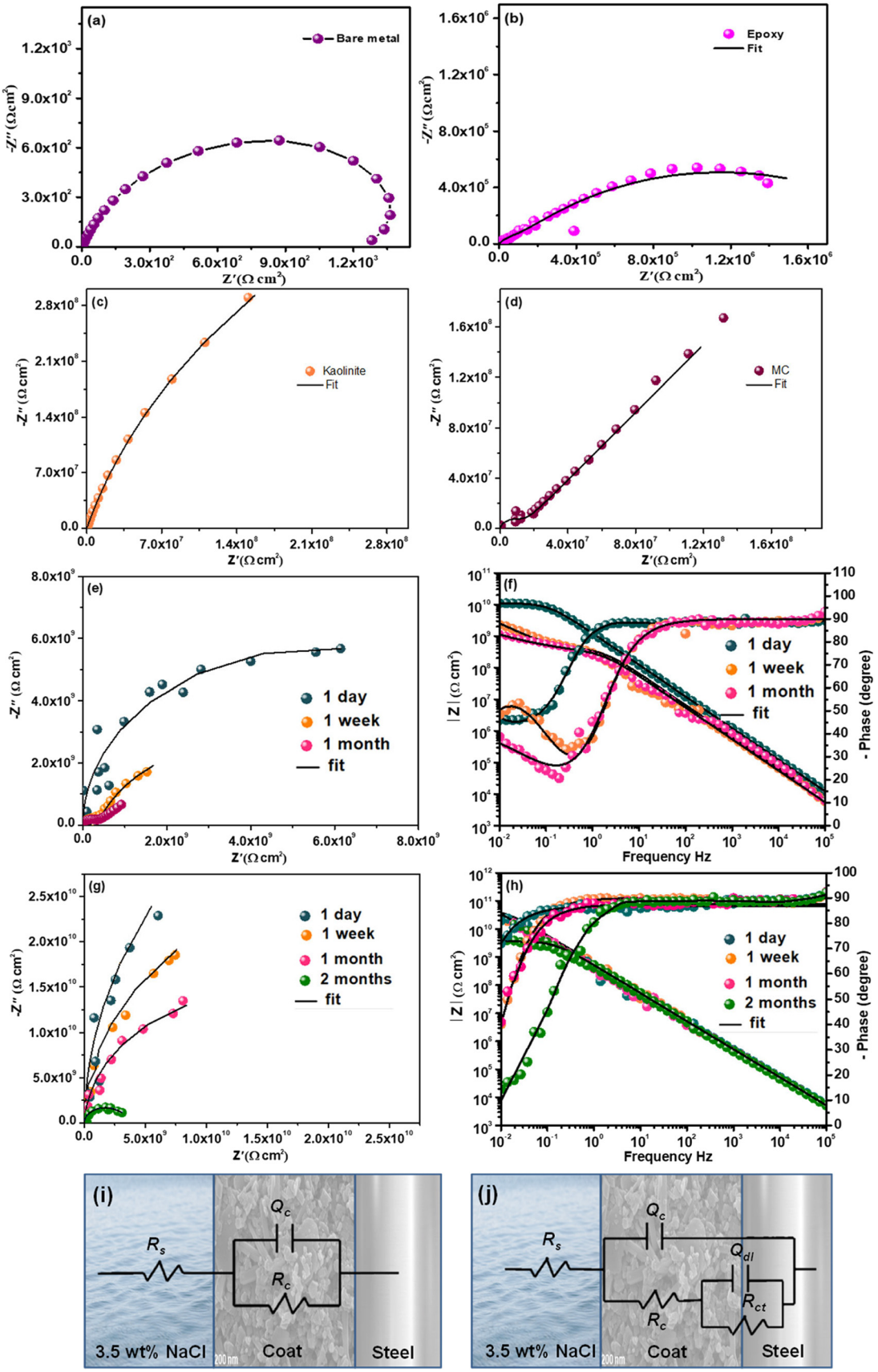

Fig. 6 Nyquist plots of (a) bare steel, (b) pristine epoxy, (c) kaolinite/epoxy, and (d) MC/epoxy and Nyquist and corresponding Bode plots of 1 wt% synthesised anticorrosive pigments with different immersion times in 3.5 wt% NaCl solution: (e and f) CeMC and (g and h) KCeMC. (i) and (j) Schematic images of the equivalent electrochemical circuit model applied to fit the experimental impedance data.

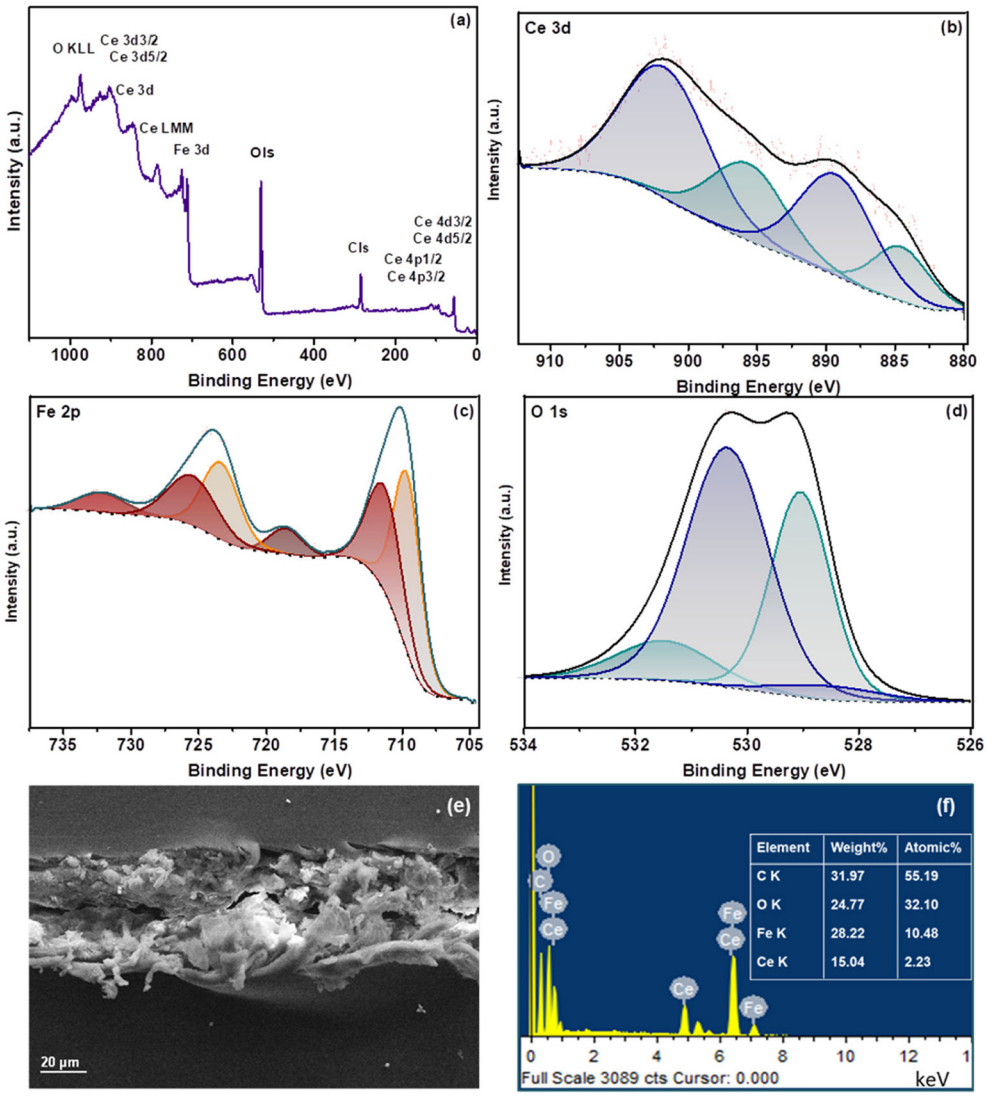

Fig. 7 XPS analysis (a) survey spectrum and core spectra of (b) Ce 3d, (c) Fe 3d and (d) O 1s, (e) SEM image, and (f) EDX spectrum from the defective site of the KCeMC/epoxy coat after exposure to a saline medium.

chemical state of the inhibitive layer. The Ce 3d core spectra depicted in Fig. 7b confirm the formation of cerium hydroxides.

Fig. 7c presents the Fe 2p spectrum, revealing peaks at 711 and 724 eV (2p3/2 and 2p1/2). The peaks are due to spin–orbit coupling. The peaks demonstrate the corrosion product Fe_3O_4. The deconvolution of the oxygen core spectra confirms the presence of Fe_3O_4 (528.3 and 531.5 eV). Further, the peaks corresponding to cerium hydroxides are at 529.0 and 530.5 eV (Fig. 7d).

An SEM micrograph of the defective KCeMC/epoxy coating after immersion in 3.5 wt% NaCl solution is presented in Fig. 7e, illustrating the film formation within the defective region. Energy-dispersive X-ray spectroscopy (EDX) was conducted at the defect site to determine the composition of the protective layer (Fig. 7f). The analysis revealed the presence of Ce, Fe, and O elements. The detected Fe and O are associated with corrosion products, whereas the presence of Ce suggests active corrosion protection imparted by the synthesised KCeMC pigment. This observation is consistent with the corrosion-inhibiting role of Ce as confirmed by the XPS analysis.

Mechanistic insight into the protection mechanism of the KCeMC/epoxy coating

The enhanced corrosion resistance of the KCeMC/epoxy coating arises from the contributions of the hybrid components kaolinite, cerium, and melamine cyanurate, and their synergistic interaction yields a durable protective coating, consistent with the EIS results. Fig. 8 presents the schematic illustration of the mechanism of protection. The major mechanistic features are summarised below.

The abundant, eco-friendly layered silicate kaolinite effectively decreases coating porosity, reducing water uptake

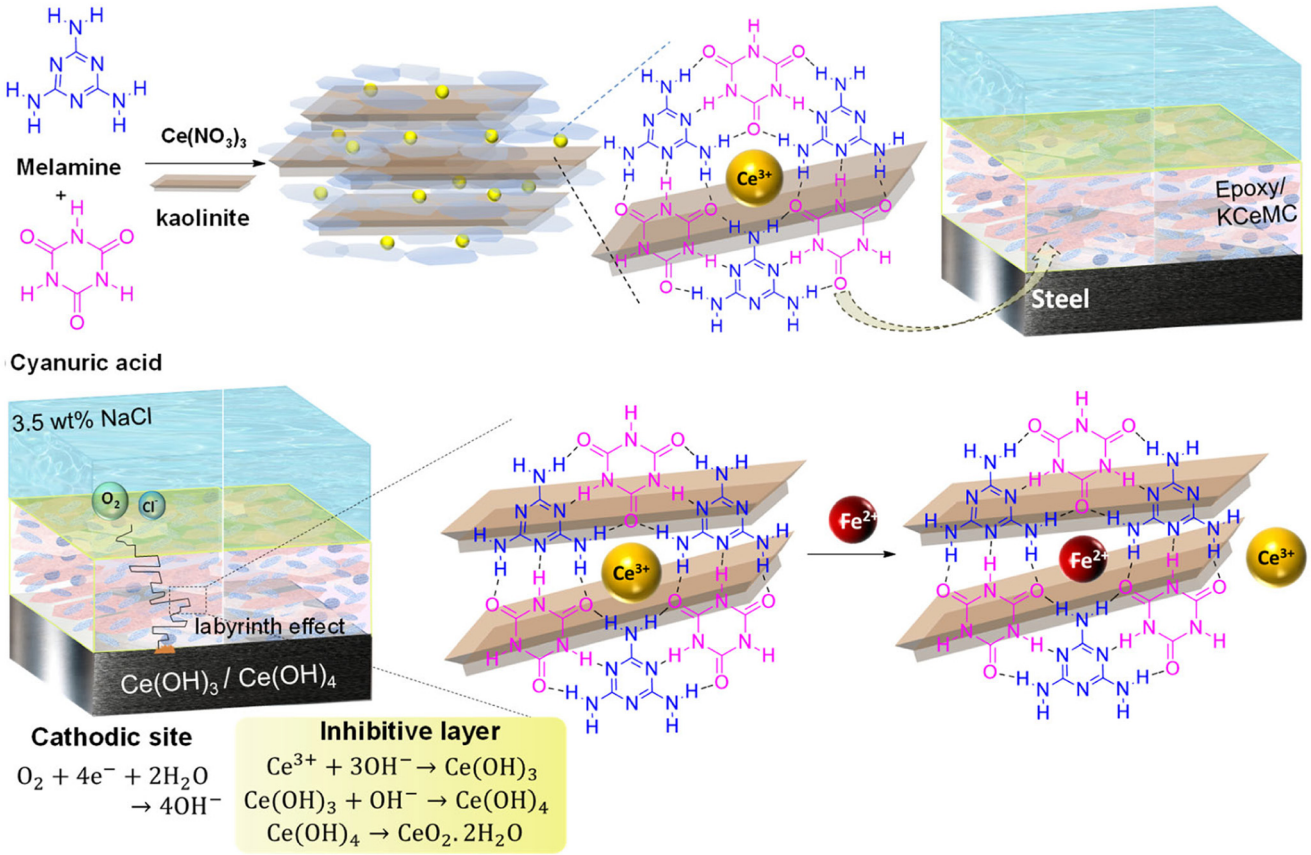

Fig. 8 Illustration outlining the mechanism of protection.

and suppressing the ingress of aggressive ions. Additionally, the flaky morphology of MC further extends the tortuous diffusion pathway, improving the barrier properties of the coating. The extended diffusion path not only increases the durability of the coating, but also enables a more controlled and persistent release of cerium ions for long-term active protection.

Kaolinite plays a crucial role in facilitating the sustainable release of cerium from the melamine cyanurate network. Upon initiation of localised corrosion, anodic dissolution occurs at defect sites, triggering the release of Ce^{3+} ions from CeMC. This release is driven by the substitution of Ce^{3+} by Fe^{2+} ions in the MC network within the coating matrix, owing to the smaller ionic radius, higher charge density, and stronger interaction of Fe^{2+} with heteroatoms of MC.

Once released, Ce^{3+} ions migrate toward cathodic regions, reacting with OH^- to form an insoluble cerium hydroxide inhibitive layer. The consumption of OH^- blocks further oxygen reduction reactions. Simultaneously, the trapping of Fe^{2+} ions in the MC network, the consumption of hydroxide ions for the protective $Ce(OH)_3$ layer, and the inherent barrier effect of the layered KCeMC morphology collectively contribute to the overall protection mechanism. The synergistic interplay between barrier enhancement (kaolinite and MC) and active inhibition ensures superior corrosion resistance of the KCeMC/epoxy system in saline environments.

Comparative analysis with commercial pigments

The synthesised pigments compared to commonly used commercial chrome and zinc-based pigments and their impedance results are shown in Table 2. The critical pigment volume concentration (CPVC) and impedance results for various commercial pigments were previously reported. Developing a pigment-free from chromium is crucial for ecological and regulatory reasons. The potential performance of the synthesised pigments compared with commercial chromium-based pigments displayed a possible promising replacement for toxic anticorrosive pigments. Current work is a hybrid pigment

Table 2 Impedance assessment with commercial pigments

Sample	CPVC (wt%)	Impedance (Ω cm^2)	References
Epoxy–KCeMC	1	1.10×10^{11}	This work
Epoxy–CeMC	1	1.14×10^{10}	This work
$ZnCrO_4$	15	3.1×10^9	38, 39
$Zn_3(PO_4)_2$	20	2.2×10^9	38, 39
$SrCrO_4$	10	4.8×10^7	38, 39

that is resistant to corrosion, free of chromium, chemically stable, and well-suited for use in harsh saline environments.

Conclusion

The present study demonstrates the superior anticorrosive performance of the synthesised KCeMC hybrid pigment incorporated epoxy coating. The hybrid pigment KCeMC effectively provides both barrier protection *via* a prolonged diffusion pathway (labyrinth effect) and active corrosion inhibition through the release of cerium cations. EIS analysis revealed that epoxy–KCeMC exhibited an exceptionally high initial R_c of 1.10×10^{11} Ω cm^2 after 1 day of saline exposure, maintaining a substantial value of 4.26×10^9 Ω cm^2 even after two months of continuous immersion, far exceeding the performance of pristine epoxy (1.63×10^5 Ω cm^2) and other pigment-loaded systems. The formation of an inhibitive cerium hydroxide layer at defect sites was validated by XPS, thus supporting the active protection of the coating system. Moreover, the synergistic combination of 2D morphological kaolinite sheets, melamine cyanurate nanoflakes, and cerium ions resulted in a denser, highly protective anticorrosive film, which consistently outperformed both pristine epoxy and other pigment-loaded coatings in aggressive saline environments. These findings suggest that KCeMC is a highly promising, chromium-free, eco-friendly anticorrosive pigment capable of extending the service life of metallic structures under harsh marine and saline conditions.

Conflicts of interest

There are no conflicts of interest to declare.

Data availability

The datasets generated during and/or analysed during the current study are not publicly available due to restrictions from the funding agency; however, they can be obtained from the authors upon reasonable request.

Acknowledgements

We thankfully acknowledge the financial support from the DST_WOS-A, Government of India (DST/WOS-A/CS-98/2021(G)). We thank Mr Peer Mohamed A and Mr Kiran Mohan, CSIR-NIIST, Thiruvananthapuram, for the XPS and TEM analysis.

References

1 K. F. Khaled and E. Ebenso, *Res. Chem. Intermed.*, 2015, **41**, 49–62.
2 N. Jayakumar and N. K. Gopalan, *J. Ind. Eng. Chem.*, 2024, **139**, 313–324.
3 N. Jayakumar, K. K. Veedu and N. K. Gopalan, *ACS Appl. Nano Mater.*, 2019, **2**, 2689–2696.
4 N. Jayakumar and N. K. Gopalan, *RSC Appl. Polym.*, 2025, **3**, 181–195.
5 Y. Dong, M. Li, Y. Zhang, C. Xie and Z. Pan, *Anti-Corros. Methods Mater.*, 2023, **70**, 59–68.
6 X. Chen, J. Tang, H. Wei, H. Zhang, Y. Tang, X. Zhao and Y. Zuo, *Coatings*, 2022, **12**, 785.
7 S. A. Haddadi, P. Najmi, N. Keshmiri, N. Tanguy, C. van der Kuur, N. Yan, T. Mekonnen and M. Arjmand, *Composites, Part B*, 2022, **239**, 109969.
8 H. Shi, E. H. Han and F. Liu, *Corros. Sci.*, 2011, **53**, 2374–2384.
9 J. Mardel, S. J. Garcia, P. A. Corrigan, T. Markley, A. E. Hughes, T. H. Muster, D. Lau, T. G. Harvey, A. M. Glenn, P. A. White, S. G. Hardin, C. Luo, X. Zhou, G. E. Thompson and J. M. C. Mol, *Prog. Org. Coat.*, 2011, **70**, 91–101.
10 M. Van Soestbergen, V. Baukh, S. J. F. Erich, H. P. Huinink and O. C. G. Adan, *Prog. Org. Coat.*, 2014, **77**, 1562–1568.
11 J. A. Zerkowski, C. T. Seto, D. A. Wierda and G. M. Whitesides, *J. Am. Chem. Soc.*, 1990, 112.
12 J. Janczak, *J. Mol. Struct.*, 2020, **1207**, 127833.
13 C. T. Seto and G. M. Whitesides, *J. Am. Chem. Soc.*, 1990, **112**, 19–84.
14 T. J. Prior, J. A. Armstrong, D. M. Benoit and K. L. Marshall, *CrystEngComm*, 2013, **15**, 5838–5843.
15 A. Ranganathan, V. R. Pedireddi and C. N. R. Rao, *J. Am. Chem. Soc.*, 1999, **121**, 1752–1753.
16 A. N. Petelski, N. M. Peruchena and G. L. Sosa, *J. Mol. Model.*, 2016, **22**, 1–10.
17 C. T. Seto and G. M. Whitesides, *J. Am. Chem. Soc.*, 1993, **115**, 1330–1340.
18 N. Orekhov, N. Kondratyuk, M. Logunov, A. Timralieva, V. Shilovskikh and E. V. Skorb, *Cryst. Growth Des.*, 2021, **21**, 1984–1992.
19 R. Rajendramani, K. Madan, M. S. N. Kallingal, S. Guru, S. De and R. R. Gangavarapu, *Langmuir*, 2023, **39**, 11992–12003.
20 X. Feng, X. Wang, W. Cai, N. Hong, Y. Hu and K. M. Liew, *J. Hazard. Mater.*, 2016, **320**, 252–264.
21 F. Jiang, R. Li, J. Cai, W. Xu, A. Cao, D. Chen, X. Zhang, C. Wang and C. Shu, *J. Mater. Chem. A*, 2015, **3**, 19433–19438.
22 Y. S. Jun, J. Park, S. U. Lee, A. Thomas, W. H. Hong and G. D. Stucky, *Angew. Chem., Int. Ed.*, 2013, **52**, 11083–11087.
23 Q. Gai, Z. Wei, S. Ren, X. Zhu, X. Zheng, W. Liu and Q. Liu, *Surf. Interfaces*, 2025, **62**, 106284.
24 V. Sangeetha, N. Kanagathara, R. Sumathi, N. Sivakumar, G. Anbalagan and C. Alvarez-Lorenzo, *J Mater.*, 2013, **2013**, 262094.
25 P. Chamorro-Posada, R. C. Dante, J. Vázquez-Cabo, D. G. Dante, P. Martín-Ramos, Ó. Rubiños-López and F. M. Sánchez-Arévalo, *J. Solid State Chem.*, 2022, **310**, 123071.
26 L. Wang, Y. Li, C. Yan, X. Li and J. He en R. Yang, *Polym.*, 2024, **16**, 2946.
27 N. Jayakumar and N. K. Gopalan, *J. Ind. Eng. Chem.*, 2024, **139**, 313–324.
28 R. Chester and H. Elderfiel, *Chem. Geol.*, 1973, **12**, 281–288.
29 D. Bougeard, K. S. Smirnov and E. Geidel, *J. Phys. Chem. B*, 2000, **104**, 9210–9217.

30 G. Jozanikohan and M. N. Abarghooei, *J. Pet. Explor. Prod. Technol.*, 2022, **12**, 2093–2106.
31 G. Fronzoni, A. Cossaro, R. Costantini, L. Di Nardi, E. Viola, G. Balducci, V. Lanzilotto and D. Toffoli, *Appl. Surf. Sci.*, 2024, **642**, 158573.
32 A. P. Koskin, Y. V. Larichev, S. A. Stepanenko, Y. V. Dubinin, A. B. Ayupov, A. A. Saraev, E. A. Suprun and P. M. Yeletsky, *C-J. Carbon Res.*, 2023, **9**, 83.
33 P. Chamorro-Posada, R. C. Dante, J. Vázquez-Cabo, D. G. Dante, P. Martín-Ramos, Ó. Rubiños-López and F. M. Sánchez-Arévalo, *J. Solid State Chem.*, 2022, **310**, 123071.
34 I. N. Reddy, B. Akkinepally, M. Dhanasekar, J. Shim and C. Bai, *Crystals*, 2024, **14**, 302.
35 T. Li, H. Liu, Y. Fan, P. Yuan, G. Shi, X. T. Bi and X. Bao, *Green Chem.*, 2012, **14**, 3255–3259.
36 P. Chamorro-Posada, R. C. Dante, J. Vázquez-Cabo, D. G. Dante, P. Martín-Ramos, Ó. Rubiños-López and F. M. Sánchez-Arévalo, *J. Solid State Chem.*, 2022, **310**, 123071.
37 A. S. de Paula, B. M. Aroeira, L. H. de O. Souza, A. C. da Cruz, M. Fedel, B. P. da Silva and F. Cotting, *Coatings*, 2024, **14**, 285.
38 K. Karattu Veedu, M. Banyangala, T. Peringattu Kalarikkal, S. B. Somappa and N. K. Gopalan, *J. Mol. Liq.*, 2023, **369**, 120967.
39 K. K. Veedu, S. Mohan, S. B. Somappa and N. K. Gopalan, *J. Cleaner Prod.*, 2022, **340**, 130750.